Analysis of a Doubly-Fed Induction Motor for Soft Start Operation Based on Stator Flux Vector Control

Warachart Suwan-ngam†, Non-member

ABSTRACT

This paper aims at analysis of an operation of a doubly-fed induction motor (DFIM). The paper mainly focuses on the soft start method for the DFIM based on stator flux vector control and the conventional topology without either circuit reconfiguration or change in the control methods. Likewise, the details about reactive power control are also discussed. With the proposed method, the DFIM can start from standstill to any speed by controlling the machine-side converter (MSC). The computer simulation is performed to a 5 kW wound rotor induction motor using PLECS software. The simulation results have successfully validated that the DFIM can operate from standstill to any speed with only a single circuit configuration and a control scheme.

Keywords: Doubly-fed Induction Motor, Soft Start, Machine-side Converter

NOMENCLATURE

L_{sl}, L_{rl}	Stator and rotor leakage inductances.
L_s, L_r	Stator and rotor self-inductances.
L_m	Three-phase magnetizing inductance.
L'_{rl}	Referred rotor leakage inductance.
R_s, R_r	Stator and rotor resistances.
R'_r	Referred rotor resistance.
τ_s, τ_r	Stator and rotor time constants.
σ	Total leakage factor.
N_s, N_r	Number of stator and rotor turns.
a	Stator-rotor turn ratio.
s	Slip.
P	Number of poles.
P_s, P_r	Stator and rotor active powers.
Q_s	Stator reactive power.
$\vec{v}_s, \vec{v}_r$	Stator and rotor voltage vectors.
$\vec{i}_s, \vec{i}_r$	Stator and rotor current vectors.
$\vec{e}_r$	Rotor induced voltage vector.
$\vec{v}'_r, \vec{i}'_r$	Referred rotor voltage and current vectors.
$\vec{v}_s^e, \vec{v}_r'^e$	Stator and referred rotor voltage vectors in stator flux reference frame.
$\vec{i}_s^e, \vec{i}_r'^e$	Stator and referred rotor current vectors in stator flux reference frame.
$\vec{i}_s^s$	Stator current vector in stationary reference frame fixed to stator.
$\vec{i}_{ms}^e$	Stator magnetizing current vector in stator flux reference frame.
$\vec{\lambda}_s^{sv}$	Stator flux vector in stationary reference frame fixed to stator calculated from voltage model.
$\vec{\lambda}_s^{si}$	Stator flux vector in stationary reference frame fixed to stator calculated from current model.
$\vec{\lambda}_s^e, \vec{\lambda}_r'^e$	Stator and referred rotor flux vectors in stator flux reference frame.
i_{sd}^e, i_{sq}^e	D-axis and Q-axis stator currents in stator flux reference frame.
$i_{rd}'^e, i_{rq}'^e$	D-axis and Q-axis rotor currents in stator flux reference frame.
$v_{rd}^{e''}, v_{rq}^{e''}$	D-axis and Q-axis PWM command voltages in stator flux reference frame.
ω_e	Stator flux speed, Synchronous speed.
ω_r, ω_{rm}	Rotor electrical and mechanical angular speeds.
ω_{sl}	Slip speed.
τ_m	Mechanical Time constant.
T_e	Electromagnetic torque.
T_L	Load torque.

1. INTRODUCTION

A doubly-fed induction machine is basically a wound rotor induction machine (WRIM) with two supplies, one at the stator and another at the rotor. The supply connected to the rotor terminal is generally an adjustable voltage and frequency source. The conventional topology is the back-to-back-converters as discussed in [1-5]. A doubly-fed induction generator (DFIG) for a wind turbine is the most successful application of the WRIM due to its reduction in converter size. However, the operation in the motor mode has been widely applied in various areas. Some applications such as pump and ship propulsion

Manuscript received on April 19, 2024; revised on July 9, 2024; accepted on August 1, 2024. This paper was recommended by Associate Editor Chainarin Ekkaravarodome.

The author is with School of Engineering, King Mongkut's Institute of Technology Ladkrabang, Ladkrabang, Bangkok, Thailand.

†Corresponding author: warachart.su@kmitl.ac.th

Digital Object Identifier: 10.37936/ecti-eec.2024223.253755

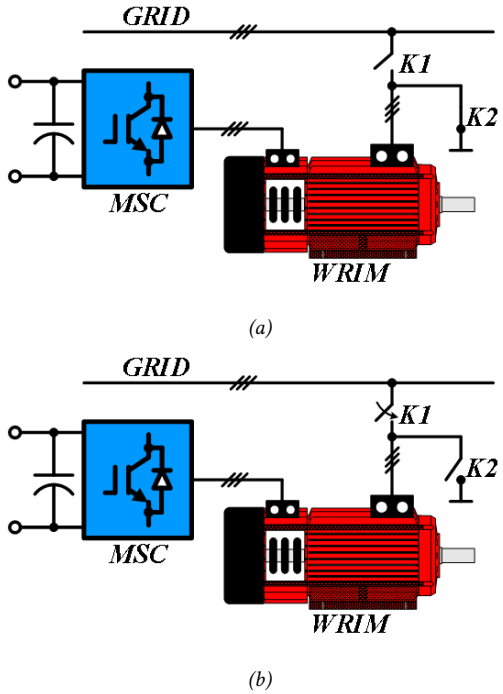

***Fig. 1**: Start-up Topologies for the DFIM Based on Driving the Rotor Circuit (a) Start-up and Acceleration Periods and (b) Grid Synchronization and Normal Operation Period.*

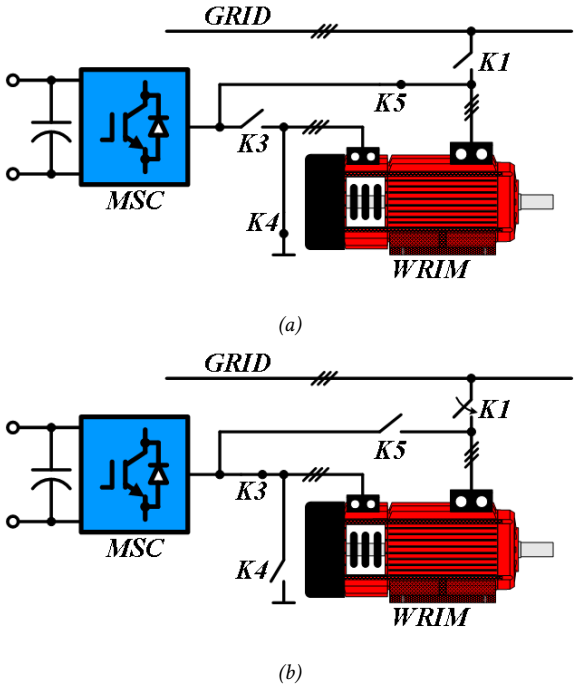

***Fig. 2**: Start-up Topologies for the DFIM Based on Driving the Stator Circuit (a) Start-up and Acceleration Period and (b) Grid Synchronization and Normal Operation Period.*

have used a doubly-fed induction motor (DFIM) as a prime mover [7-21].

Operation in the motor mode requires a start-up method to accelerate the rotor from a standstill. Several methods have been proposed and some are commonly used nowadays. Most of them require circuit reconfiguration from start-up to normal operation. The most applicable method is to use the machine-side converter (MSC) to control the rotor circuit while short circuiting the stator circuit as shown in Fig.1a [8-15]. Two induction motor control methods are proposed to control the MSC such as the constant V/F and stator flux vector controls. This allows the DFIM to start and accelerate to a specific speed in sub-synchronous speed region. Once the speed is stabilized, the MSC is stopped, and the stator circuit is opened. The grid synchronization process is then performed. During this state, the contactor K1 in Fig.1b is kept open. The operation during this period is the same as that used for the DFIG. Once this step is completed, the contactor K1 is closed and the MSC starts its operation under vector control mode.

An alternative starting topology is based on short circuiting the rotor circuit and connecting the MSC to the stator circuit as depicted in Fig.2a [10,16]. In this topology, the DFIM is controlled by the rotor flux vector control as applied to a squirrel cage rotor motor. The motor can start and accelerate to a specific speed as in the previous case. After acceleration, the MSC is stopped, and the circuit is reconfigured as shown in Fig.2b. The contactor K1 is kept open for grid synchronization process. After grid synchronization, the contactor K1 is

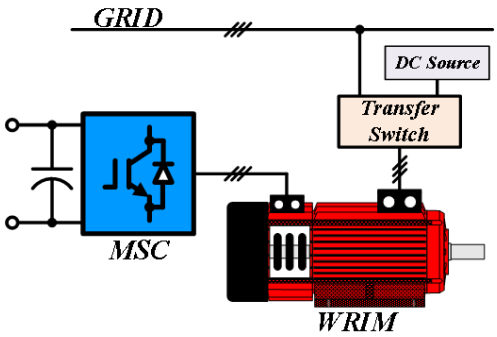

***Fig. 3**: Start-up Topologies for the DFIM Based on Switched Supplies.*

closed and the DFIM operates under stator flux vector control.

A notable aspect of these two methods is that the MSC must be temporarily stopped, and circuit reconfiguration is required before grid synchronization. During this period, the DFIM runs without control, causing speed deceleration depending on the mechanical time constant of the system. However, most applications found in several research are based on a high inertia system, so the speed change is insignificant.

A. Banerjee *et al.* proposed a start-up procedure by applying a DC voltage source to the stator and operate the DFIM as a wound-field synchronous motor (WFSM) as depicted in Fig. 3. The MSC is driving the DFIM under the stator flux vector control [17, 18]. This method requires a transition from a DC source to an AC source,

and the results show a smooth speed transition.

The start-up methods relying on the operation of the MSC have also been proposed [19-21]. However, they require specific control until the speed reaches the specific value to switch to either grid flux or stator flux vector control.

The start-up strategy for the DFIM can also be achieved by using the converter connected to the stator circuit, resulting in a dual converter topology[22-33]. This topology benefits the four-quadrant operation of the DFIM due to the control provided by the stator-side converter (SSC). The SSC is responsible for the start-up process while the MSC is responsible for controlling the rotor flux of the DFIM. Several controls have been proposed to synchronize the operation of both SSC and MSC.

Although starting the DFIM from standstill is possible, they require either circuit reconfiguration or change in control methods. It would be better to successfully operate the DFIM under single configuration and control scheme. Therefore, this paper mainly focuses on the proposed technique to start and accelerate the DFIM from standstill to the desired operating speeds based on the conventional topology and stator flux vector control. A step-by-step operation is graphically explained in the form of a flowchart and control diagrams. In addition, an alternative method to calibrate the encoder for correcting the initial position of the rotor is also proposed. This paper begins with a discussion of a DFIM and its control, including an explanation of the stator reactive power control for the DFIM in Section 2. Section 3 focuses the proposed soft start criteria based on the conventional topology. The initial encoder calibration is also discussed in this section. The proposed soft start method and proposed encoder calibration are validated through simulation using PLECS software as will be discussed in Section 4. The simulation results are presented and discussed in Section 5. Finally, the conclusion is then presented in Section 6.

2. A DOUBLY-FED INDUCTION MOTOR

A WRIM has a wound rotor having its rotor terminal connected to the slip ring as illustrated in Fig. 4, so the rotor circuit is accessible. This machine has the complex equivalent circuit as depicted in Fig. 5. The WRIM can also be applied as a frequency converter based on operating speed of the rotor as well as a three-phase transformer having the airgap between the primary and secondary circuits. The complex equivalent circuit shown in Fig. 5 is based on the non-referred dynamic voltage equations in a synchronous reference frame described in equations (1) and (2),

$$\vec{v}_s = R_s \vec{i}_s + L_{sl}(p + j\omega_e)\vec{i}_s + L_m(p + j\omega_e)(\vec{i}_s + \vec{i}'_r), \quad (1)$$

$$\vec{v}_r = R_r \vec{i}_r + L_{rl}(p + js\omega_e)\vec{i}_r + \vec{e}_r. \quad (2)$$

The rotor voltage level is the function of the stator-rotor turn ratio and the slip as can be explained in equation (3),

$$v'_r = s\left(\frac{N_r}{N_s}\right)v_s = \left(\frac{s}{a}\right)v_s. \quad (3)$$

Moreover, the relationship between the stator active power and the rotor active power is described in equation (4),

$$P_r = -sP_s. \quad (4)$$

The rotor power flow direction depends on the operating speed regions of the motor which can be classified into 3 regions such as, sub-synchronous, synchronous, and super-synchronous speed regions as depicted in Fig.6.

To achieve the operation in these speed ranges, a four-quadrant converter is required to connect to the rotor. The WRIM with the back-to-back converters connected at the rotor is the most applicable topology, as shown in Fig.7. These converters consist of two PWM converters connected back-to-back. One connected to the rotor terminal is called the machine-side converter (MSC) while another connected to the grid is called the grid-side converter (GSC). The MSC is responsible for controlling the WRIM while the GSC is responsible for regulating the DC-link voltage and reactive power control of the converter.

In Fig. 7, there is a three-phase transformer connected between the GSC and the grid. The transformer is optional depending on the design of the WRIM. It is required if the rotor open circuit voltage is much lower than the grid voltage leading to low DC-link voltage.

The topology shown in Fig.7 is well known for electricity generation from wind turbines and it is called a DFIG. The advantage of the DFIG over other generators is a reduction in converter sizes [1-5]. However, for motor application, regardless of the restriction of the converter size, the WRIM can operate 2 times of the base speed without field weakening. Several vector control schemes have been proposed, for example, stator flux vector control, grid flux vector control, magnetizing flux vector control and rotor flux vector control. However, in this paper, only the stator flux vector control for the MSC is considered.

2.1 Stator Flux Vector Control

A doubly-fed induction machine is typically used in the generator mode as a DFIG. The grid flux vector control using a virtual grid flux as a reference frame is generally applied to directly control the stator active and reactive powers via control of the rotor current. However, in the case of the DFIM, the main requirement is to control the torque and flux, as generally required for motor applications. Therefore, the control reference frame is aligned with the stator flux vector, which is known as the stator flux vector control. The vector diagram of the rotor current vector and the necessary reference frame is shown in Fig.8. The stator flux vector

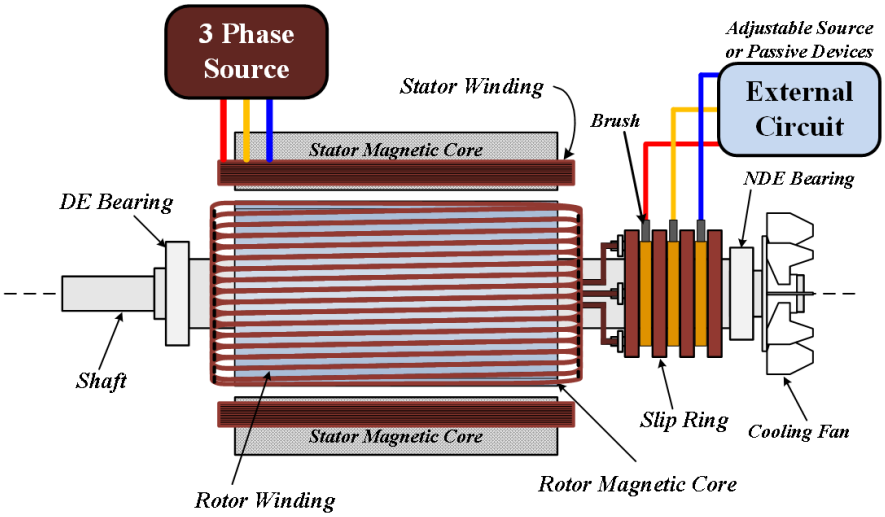

***Fig. 4**: Structure of a Wound Rotor Induction Machine.*

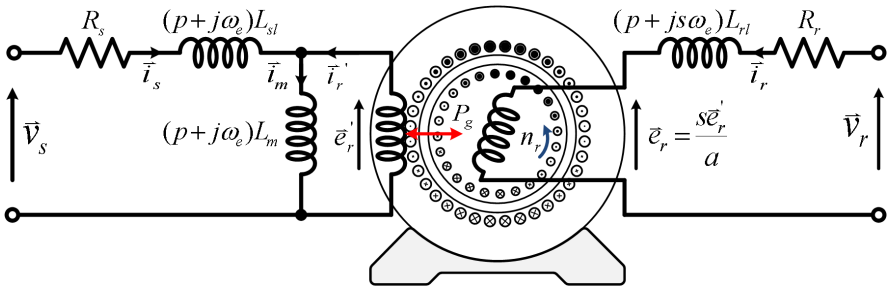

***Fig. 5**: Complex Equivalent Circuit of a Wound Rotor Induction Machine.*

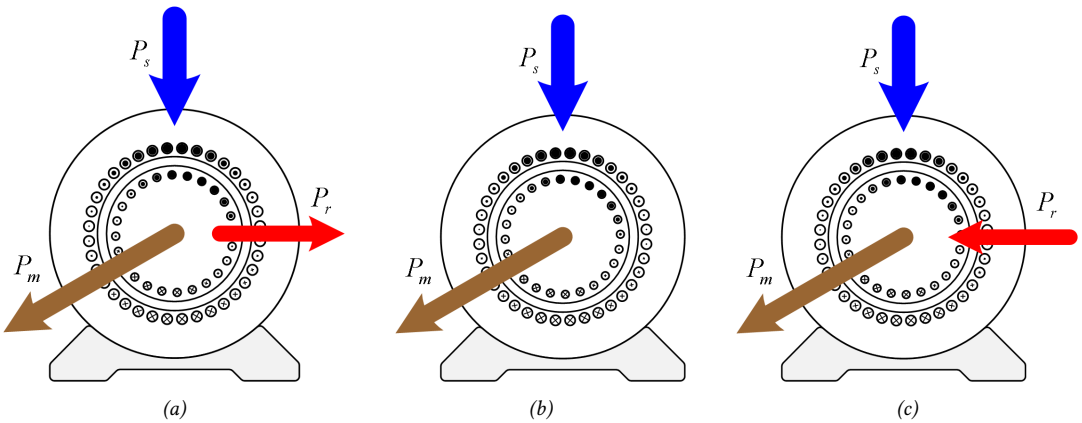

***Fig. 6**: Active Power Flow Diagram of a DFIM for Operation in Different Speed Regions, (a) Sub-Synchronous Speed, (b) Synchronous Speed, and (c) Super-Synchronous Speed.*

can be written in the form of the stator magnetizing current as described in equation (5),

$$\vec{\lambda}_s^e = L_m \vec{i}_{ms}^e = L_s \vec{i}_s^e + L_m \vec{i}_r'^e \tag{5}$$

Since the control occurs at the rotor side, the stator current is not in used. Therefore, the stator current vector can be replaced by $\vec{i}_{ms}^e$ and $\vec{i}_r'^e$ as shown in equation (6),

$$\vec{i}_s^e = \frac{L_m}{L_s}(\vec{i}_{ms}^e - \vec{i}_r'^e). \tag{6}$$

The stator current vector can then be separated into d-axis and q-axis components as shown in equations (7) and (8) respectively,

$$i_{sd}^e = \frac{L_m}{L_s}\left(\left|\vec{i}_{ms}^e\right| - i_{rd}'^e\right), \tag{7}$$

$$i_{sq}^e = -\frac{L_m}{L_s} i_{rq}'^e. \tag{8}$$

In the stator flux reference frame, the rotor and stator

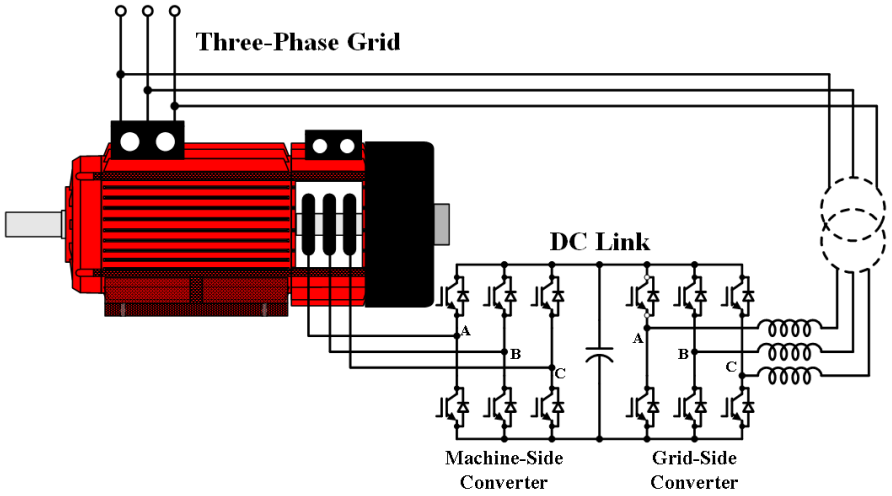

***Fig. 7**: Topology of a Doubly-Fed Induction Machine.*

voltage vector equations are presented in equations (9) and (10) respectively.

$$\vec{v}_r'^e = R_r'\vec{i}_r'^e + \frac{d\vec{\lambda}_r'^e}{dt} + j(\omega_e - \omega_r)\vec{\lambda}_r'^e \tag{9}$$

$$\vec{v}_s^e = R_s\vec{i}_s^e + \frac{d\vec{\lambda}_s^e}{dt} + j\omega_e\vec{\lambda}_s^e. \tag{10}$$

These equations can be arranged in the 1^{st} order differential equation form as shown in (11) and (12) respectively,

$$\sigma\tau_r\frac{d\vec{i}_r'^e}{dt} + \vec{i}_r'^e = \frac{\vec{v}_r'^e}{R_r'} - j\omega_{sl}\sigma\tau_r\vec{i}_r'^e - (1-\sigma)\tau_r\left(\frac{d\vec{i}_{ms}^e}{dt} + j\omega_{sl}\vec{i}_{ms}^e\right), \tag{11}$$

$$\tau_s\frac{d\vec{i}_{ms}^e}{dt} + \vec{i}_{ms}^e = \tau_s\frac{\vec{v}_s^e}{L_m} + \vec{i}_r'^e - j\omega_e\tau_s\vec{i}_{ms}^e \tag{12}$$

where $\sigma = 1 - \frac{L_m^2}{L_sL_r'}$, and $\omega_{sl} = \omega_e - \omega_r$.

Equations (11) and (12) can be separated into the d-axis and q-axis components as shown in equations (13)-(16) respectively. Likewise, the electromagnetic torque, reactive power and mechanical dynamic equations are presented in equations (17)-(19) respectively. The DFIM under stator flux vector control can be modelled in the form of transfer function as depicted in Fig.9 based on equations (13)-(19),

$$\sigma\tau_r\frac{di_{rd}'^e}{dt} + i_{rd}'^e = \frac{v_{rd}'^e}{R_r'} + \omega_{sl}\sigma\tau_r i_{rq}'^e - (1-\sigma)\tau_r\frac{d\left|\vec{i}_{ms}^e\right|}{dt} \tag{13}$$

$$\sigma\tau_r\frac{di_{rq}'^e}{dt} + i_{rq}'^e = \frac{v_{rq}'^e}{R_r'} - \omega_{sl}\sigma\tau_r i_{rd}'^e - \omega_{sl}(1-\sigma)\tau_r\left|\vec{i}_{ms}^e\right| \tag{14}$$

$$\tau_s\frac{d\left|\vec{i}_{ms}^e\right|}{dt} + \left|\vec{i}_{ms}^e\right| = \tau_s\frac{v_{sd}^e}{L_m} + i_{rd}'^e, \tag{15}$$

$$v_{sq}^e = \omega_e L_m\left|\vec{i}_{ms}^e\right| - \frac{L_m}{L_s}R_s i_{rq}'^e \tag{16}$$

$$T_e = -\frac{P}{2}\frac{3}{2}\frac{L_m^2}{L_s}\left|\vec{i}_{ms}^e\right|i_{rq}'^e \tag{17}$$

$$Q_s = \omega_e\frac{P}{2}\frac{3}{2}\frac{L_m^2}{L_s}\left|\vec{i}_{ms}^e\right|\left(\left|\vec{i}_{ms}^e\right| - i_{rd}'^e\right) \tag{18}$$

$$\tau_m\frac{d\omega_{rm}}{dt} + \omega_{rm} = T_e - T_L \tag{19}$$

The block diagram in Fig. 9 is also useful for tuning the controller and analysing the behaviour of the DFIM-based stator flux vector control.

According to equations (13) and (14), the last two terms on the right-hand side of both equations are the cross-coupling voltages which prevent decouple control. They must be eliminated in the control process. The method presented in this paper is the feed-forward compensation [1-3] having an equation for each axis shown in equations (20) and (21) respectively. The control diagram of the DFIM is depicted in Fig.10.

$$v_{comp\_d} = -\omega_{sl}\sigma\tau_r i_{rq}'^e + (1-\sigma)\tau_r\frac{d\left|\vec{i}_{ms}^e\right|}{dt} \tag{20}$$

$$v_{comp\_q} = \omega_{sl}\sigma\tau_r i_{rd}'^e + \omega_{sl}(1-\sigma)\tau_r\left|\vec{i}_{ms}^e\right| \tag{21}$$

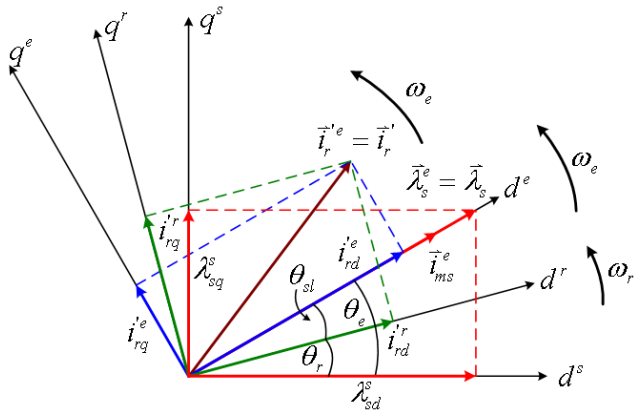

***Fig. 8**: Vector Diagram of the Rotor Current under the Stator Flux Vector Control for the DFIM.*

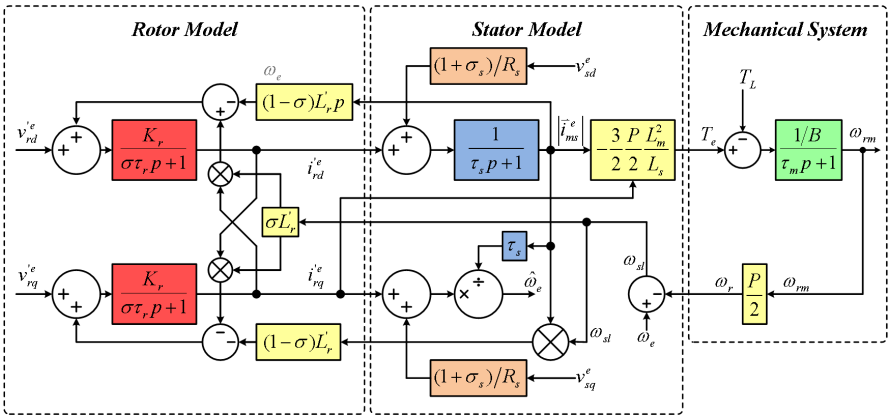

***Fig. 9**: A Complete Transfer Function of a DFIM in the Stator Flux Reference Frame.*

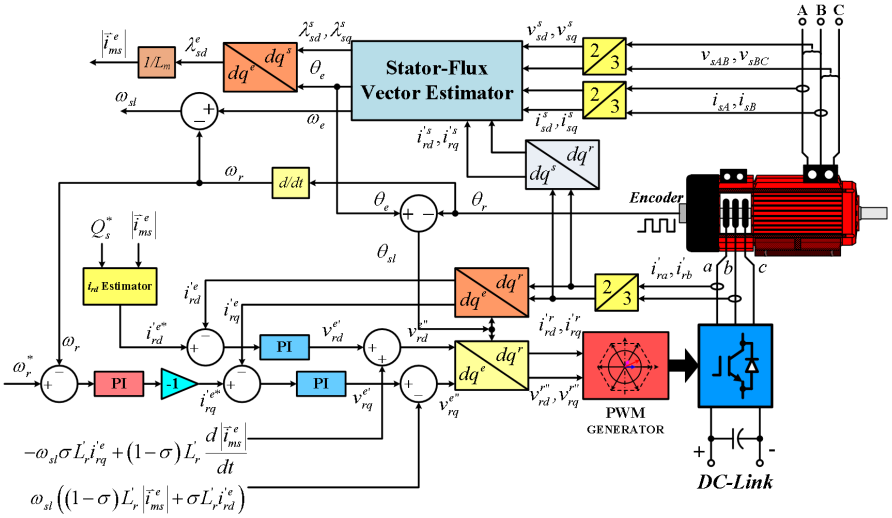

***Fig. 10**: Control Diagram of the DFIM.*

2.2 Stator Flux Vector Estimation

The most important part of the vector control for the rotating machine is the reference frame estimation. Therefore, in this case, stator flux vector estimation must be performed. Theoretically, estimation using voltage model is an ideal method because it is less parameter dependent and requires only a single integrator. Unfortunately, in practice, this method suffers from a small DC offset resulting in divergence of the integration result [34]. Several methods have been proposed to solve this problem, for example: a discrete low pass filter with low cut-off frequency method. However, it does not provide good results. Therefore, in this paper, the

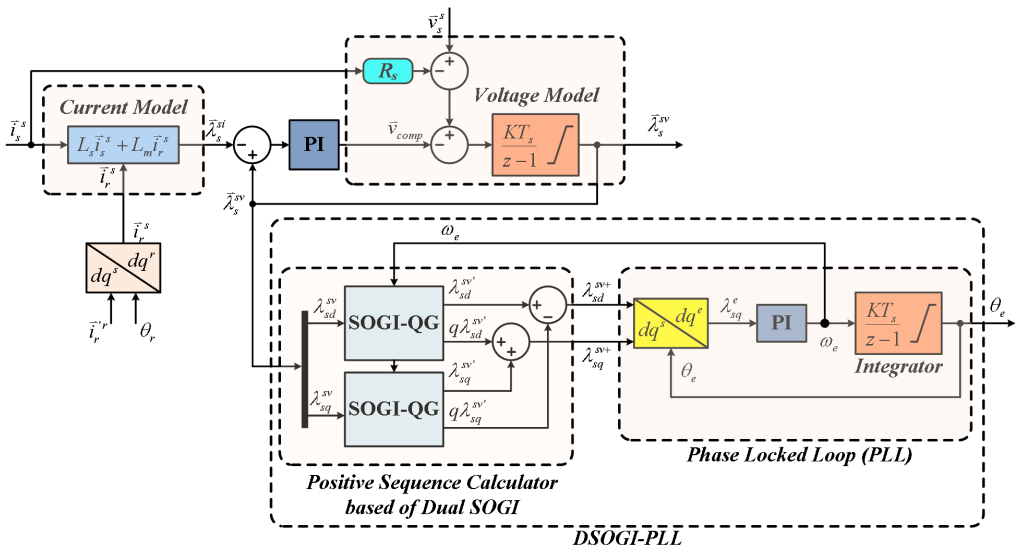

***Fig. 11**: Stator Flux Vector Estimation Block Diagram with DSOGI-PLL.*

adaptive method based on the voltage and current models is adopted [34, 35]. The equations for the stator flux vector estimation using voltage and current models are described in equations (22) and (23) respectively,

$$\vec{\lambda}_s^{sv} = \int (\vec{v}_s^s - R_s \vec{i}_s^s)dt \tag{22}$$

$$\vec{\lambda}_s^{si} = L_s \vec{i}_s^s + L_m \vec{i}_r'^s \tag{23}$$

This method uses the voltage model as the reference model while the current model is applied to calculate the compensating voltage vector as described in equation (24),

$$\vec{v}_{comp} = K_p(\vec{\lambda}_s^{sv} - \vec{\lambda}_s^{si}) + K_i \int (\vec{\lambda}_s^{sv} - \vec{\lambda}_s^{si})dt \tag{24}$$

From (24), K_p and $K_i$can be calculated from equations (25) and (26) respectively,

$$K_p = \omega_1 + \omega_2 \tag{25}$$

$$K_i = \omega_1 \cdot \omega_2 \tag{26}$$

where ω_1 = 2-5 rad/s, and ω_2 = 20-30 rad/s [35].

Finally, the stator flux vector can be estimated using equation (27),

$$\vec{\lambda}_s^{sv} = \int (\vec{v}_s^s - R_s \vec{i}_s^s - \vec{v}_{comp})dt \tag{27}$$

where $\vec{v}_{comp}$ is a compensating voltage vector from equation (24).

The process of the stator flux vector estimation following equations (23)-(27) is depicted at the top of Fig. 11. It results in the stator flux vector estimated in the stationary reference frame fixed to stator. The estimation of the position and the angular frequency can be achieved by a three-phase phase-locked loop (PLL) called a general dq-PLL which is suitable only for the case that the DFIM is connected to a clean and balanced three-phase source. However, in practice, the three-phase grid voltage is hardly balanced. This imbalance causes an oscillation in the stator flux vector estimated in its own reference frame. The effective solution is to extract the positive sequence components from the stator flux waveforms and feed them to the general dq-PLL. It is the same as the method applied for the voltage waveforms for the grid connected converter [36].

A dual second-order generalize integrator (DSOGI) is one of the effective methods for extracting the positive sequence components from the stator flux waveforms [36]. The combination of the DSOGI and the general dq-PLL is called a dual second-order generalize integrator-PLL (DSOGI-PLL). It is selected to estimate the position and angular frequency of the stator flux vector as shown at the bottom of Fig.11.

2.3 Stator Reactive Power Control

The DFIM can be called the generalized motor because it can be operated as either an asynchronous motor or a wound field synchronous motor (WFSM). In the case of the WFSM, the rotor converter is generally responsible for control of the field circuit resulting in the stator reactive power control. Unlike the case of WFSM, the MSC is responsible for both stator active and reactive powers.

In the case of the stator reactive power control, the d-axis differential equation of the stator magnetizing current vector $\vec{i}_{ms}^e$ is considered. The equation is in the form of equation (28),

$$\tau_s \frac{d\left|\vec{i}_{ms}^e\right|}{dt} + \left|\vec{i}_{ms}^e\right| = \tau_s \frac{v_{sd}^e}{L_m} + i_{rd}'^e \tag{28}$$

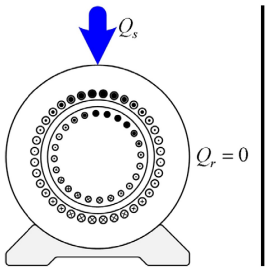

***Fig. 12**: Reactive Power Flow Diagram of the DFIM while Exciting via the Stator Circuit Only.*

During the transient state, change in either d-axis stator voltage or d-axis rotor current results in first order response of the stator flux linkage. However, at steady state, the stator magnetizing current depends on either I^{e}_{sd}or I'^{e}_{rd}.as described in equation (29),

$$\left|\vec{I}^{e}_{ms}\right| = \tau_s \frac{V^{e}_{sd}}{L_m} + I'^{e}_{rd} = \frac{L_s}{L_m} I^{e}_{sd} + I'^{e}_{rd} \tag{29}$$

The stator reactive power control can be categorized into 4 cases.

Case 1: The d-axis rotor current is controlled to be zero, $I'^{e}_{rd} = 0$, the DFIM is magnetized via the stator circuit only. The stator circuit consumes reactive power while the reactive power exchanged between the rotor circuit and the source is zero. This case is like the operation of a squirrel cage induction motor (SCIM), and the reactive power flow diagram is depicted in Fig.12.

Case 2: The DFIM is magnetized via both stator and rotor circuits to generate $\vec{\lambda}^{e}_{s}$. Both terms on the right-hand side of equation (29) are higher than 0, $I'^{e}_{rd} > 0$ and $\frac{L_s}{L_m} I^{e}_{sd} > 0$. Therefore, the DFIM consumes the reactive power from both stator and rotor supplies. Operation in this case is like an under excited synchronous motor, and the reactive power flow diagram is depicted in Fig.13.

Case 3: The DFIM is magnetized via the rotor circuit only to generate $\vec{\lambda}^{e}_{s}$, meaning that $I'^{e}_{rd} = \left|\vec{I}^{e}_{ms}\right|$ and $\frac{L_s}{L_m} I^{e}_{sd} = 0$. Therefore, the DFIM consumes the reactive power from the rotor supply only, so the stator power factor becomes unity. Operation in this case is like a normal excited synchronous motor, and the reactive power flow diagram is depicted in Fig. 14.

Case 4: The DFIM is over excited via the rotor circuit, therefore, the $\vec{\lambda}^{e}_{s}$ is generated by I'^{e}_{rd} and the excess is push out to the stator supply in the form of reactive power. Therefore, from (29), $I'^{e}_{rd} > 0$ but $\frac{L_s}{L_m} I^{e}_{sd} < 0$. Operation in this case is like an over excited synchronous motor, and the reactive power flow diagram is depicted in Fig. 15.

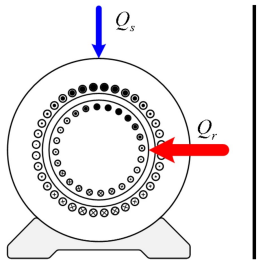

***Fig. 13**: Reactive Power Flow Diagram of the DFIM while Exciting via Both Stator and Rotor Circuits.*

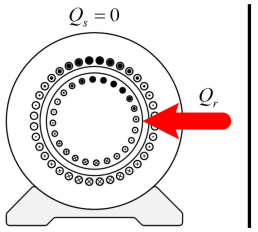

***Fig. 14**: Reactive Power Flow Diagram of the DFIM while Exciting via the Rotor Circuit Only.*

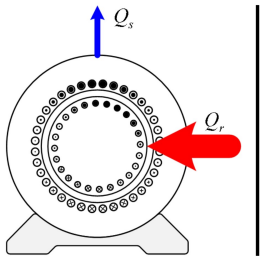

***Fig. 15**: Reactive Power Flow Diagram of the DFIM while Over Exciting at the Rotor Circuit.*

3. PROPOSED SOFT START OPERATION

This section mainly focuses on detail explanation of the proposed soft start method based on control of the MSC. The more detail about an alternative initial rotor position correction is also discussed.

3.1 Operating Sequence for Soft Start

The operation of the DFIM is different from the DFIG in the way that it mostly starts from standstill and can drive the load. The proposed operating sequence is required to avoid starting failure or too high starting current. The converter rating is also considered. According to the rotor voltage and power equations in (3) and (4), at standstill, the rotor voltage and active power is equal to those of the stator. Therefore, to achieve the proposed soft start method, the converter voltage rating must be as high as rotor terminal voltage.

The flowchart describing the operating sequence is shown in Fig. 16 as well as the diagram containing the operating sequence as described in the flowchart is illustrated in Fig. 17. There are 4 steps for the soft start operation. Each step is labeled by the number in the

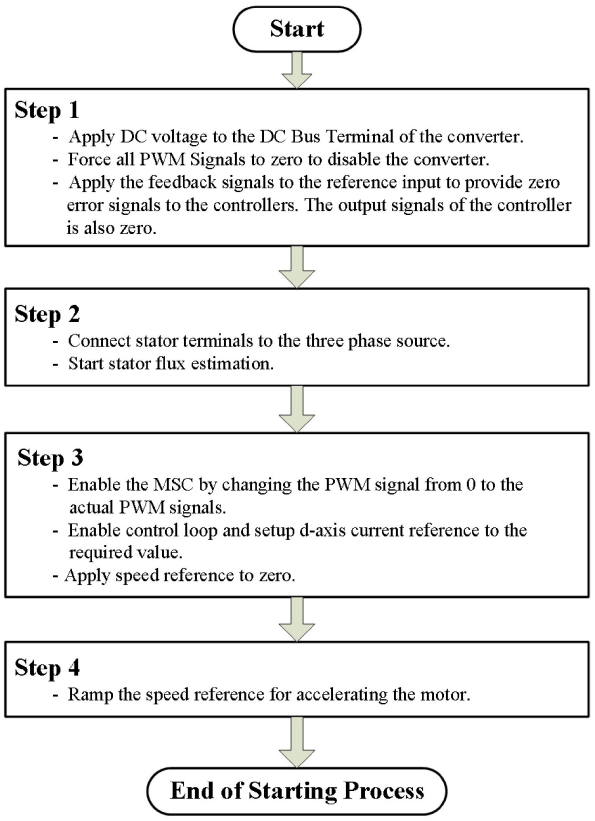

***Fig. 16**: A Flowchart Showing the Operating Sequence for Soft Start of the DFIM.*

circle.

The 1^{st} step: The converter PWM signals are forced to zero to disable the converter while the DC Voltage is applied to the DC bus. The feedback signal of each control loop is set to be the reference signal for the controller to prevent controller saturation.

The 2^{nd} step: The stator is connected to the three-phase source. This condition is like connecting the transformer to the grid at no load. Once the stator current is steady, the stator flux estimation process is performed. During this step, the PWM signal is generated, and the voltage command is from the compensating voltages only as in equations (30) and (31) respectively,

$$v_{rd}^{e''} = (1-\sigma)\tau_r \frac{d\left|\vec{i}_{ms}^{\,e}\right|}{dt} \tag{30}$$

$$v_{rq}^{e''} = \omega_{sl}(1-\sigma)\tau_r \left|\vec{i}_{ms}^{\,e}\right| \tag{31}$$

Meanwhile, all switches are still forced to OFF.

The 3^{rd} step: The MSC is enabled by applying the actual PWM signal to the converter. At the same time, all controllers are enabled by changing the reference command from their feedback signal to the actual reference signal as shown in Fig. 17b. At this point, the control diagram is the same as that shown in Fig.8. and ready for the 4^{th} step to accelerate the DFIM.

The 4^{th} step: The DFIM is accelerating to the desired speed following the command and continuously operating until the end of operation.

3.2 Initial Rotor Position Correction

The initial rotor position is the serious issue that must be addressed. In simulation, the initial rotor position is set to zero by default. However, the rotor position is practically acquired from the position sensor; for example, an incremental encoder, but it can provide only the relative position value. The correct rotor position must align with the rotor flux vector, otherwise the stator flux vector control will fail. The rotor position can be described in equation (32),

$$\theta_{r\_new}(t) = \theta_r(t) + \theta_{r\_comp} \tag{32}$$

where $\theta_r(t)$ is the pre-correction rotor position, $\theta_{r\_new}(t)$ is the corrected rotor position, and θ_{r_comp},is the compensating angle.

The $\theta_r(t)$ is calculated from the encoder pulses resulting in the relative rotor position. It is not readily used for stator flux vector control. Therefore, θ_{r_comp} must be calculated to correct the rotor position. Typically, θ_{r_comp} is calculated using the stator flux vector equation [3, 10]. This method is generally applied to the DFIG, and it is performed while the rotor is driven by a prime mover. Meanwhile, the MSC connected to the rotor is controlled by grid voltage vector control [3] to excite the DFIG.

This paper proposes an alternative method to calculate θ_{r_comp} based on the rotor flux vector,$\vec{\lambda}_r^{\,s}$. The correction is performed by connecting the stator to the three-phase source while the rotor is open-circuited. The rotor flux linkage can be calculated from both current and voltage models in the stationary reference frame fixed to stator as described in (33) and (34) respectively,

$$\vec{\lambda}_{ri}^{\,'s} = L_r^{'s}\vec{i}_r^{\,'s} + L_m\vec{i}_s^{\,s} \tag{33}$$

$$\vec{\lambda}_{rv}^{\,'s} = \int (\vec{v}_r^{\,s} - R_r^{'}\vec{i}_r^{\,'s} + j\omega_r\vec{\lambda}_r^{\,'s})dt \tag{34}$$

During the calibration process, the rotor terminal is open circuited, so the equation of the $\vec{\lambda}_{ri}^{\,'s}$ is reduced to equation (35) and is dependent on the stator current vector only. In the case of the $\vec{\lambda}_{rv}^{\,'s}$, the equation is reduced to (36). In this case, the vector of the terminal voltage is the same as the vector of the induced voltage. It can be said that the $\vec{\lambda}_{rv}^{\,'s}$ is the virtual rotor flux linkage,

$$\vec{\lambda}_{ri\_open}^{\,'s} = L_m\vec{i}_s^{\,s} \tag{35}$$

$$\vec{\lambda}_{rv\_open}^{\,'s} = \int \vec{v}_r^{\,s}dt \tag{36}$$

Considering equation (35), the position of the rotor flux linkage vector, $\vec{\lambda}'^{s}_{ri\_open}$ is the same as that of the stator current vector and can be symbolized $\theta_{\lambda i}(t)$. This position is independent of the rotor position because it is calculated from the stator variable which is at rest referring to the stationary reference frame fixed to stator. This position was selected to be the reference position of the rotor flux linkage.

Conversely, $\theta_{\lambda v}(t)$, which is the position of $\vec{\lambda}'^{s}_{rv\_open}$, is 90 degrees behind $\theta_v(t)$ which is the position of the rotor voltage vector $\vec{v}'^{s}_{rv}$. Therefore, the virtual rotor flux position can be calculated from equation (37),

$$\theta_{\lambda v}(t) = \theta_v(t) - 90^{\circ}. \tag{37}$$

The $\theta_{\lambda v}(t)$ is depending on the rotor position because the rotor flux vector is calculated from the rotor terminal which has the relative position referring to the stationary reference frame fixed to stator. Therefore, the error of the rotor position can be calculated as follows,

$$\Delta\theta_r = \theta_{\lambda i}(t) - \theta_{\lambda v}(t). \tag{38}$$

This value is then used for correcting the absolute rotor position $\theta_{r\_new}(t)$ in equation (32). The relationship between θ_{r_comp} and $\Delta\theta_r(t)$ is shown in equation (39),

$$\theta_{r\_comp} = -\Delta\theta_r(t) \tag{39}$$

4. SIMULATION AND SIMULATION RESULTS

The computer simulations were performed to validate the proposed soft-start operation and the initial rotor position correction. The simulations were performed to the 5 kW wound rotor induction machine having the variables and parameters as shown in Table 1

4.1 Simulation System

The simulations were performed using PLECS software. The 1^{st} simulation system is the soft-start operation based on the stator flux vector control of the MSC as shown in Fig.18.

The DFIM model is supplied by a 400V 50 Hz three-phase source. In this case, the mechanical input of the WRIM model is set to torque input. The MSC is controlled with the sampling rate at 10 kHz, while the switching frequency is set to 5 kHz. As a result, the PWM signal is updated twice for each switching period. For ease of following the simulation process and the results, the simulation process is summarized as shown Table 2. At the time 5 s., the speed command is ramped with the ramp rate at different ramp rates.

The 2^{nd} simulation system is the initial rotor position correction. The mechanical input of the WRIM model is set to the speed input to manually control the rotational speed of the motor. The rotor circuit is connected to three high value resistors to simulate an open circuit as shown in Fig.19. The simulations of the initial rotor position correction were performed under different error angles and rotor speeds.

***Table 1**: Parameters of a WRIM.*

Parameter	Value	Unit
Stator Rated Voltage	400	V
Rotor Rated Voltage	200	V
Stator Rated Current	9.7	A
Rotor Rated Current	11.4	A
Base Frequency	50	Hz
Base Speed	1500	rpm
Number of Poles	4	Poles
Stator-Rotor Turn Ratio	2	
Stator Resistance	1.0972	Ω
Referred Rotor Resistance	2.0250	Ω
Stator Self Inductance	0.203642	H
Referred Rotor Self Inductance	0.203642	H
Magnetizing Inductance	0.195853	H
Moment of Inertia	0.018	Kg-m^2
Viscous Friction Coefficient	0.008242	Nm s/Rad
DC Bus Voltage	300	V

***Table 2**: Simulation Process.*

Time (s)	Process
0.75	Connect Stator to the Grid
1.50	Enable Stator Flux Estimation
2.00	Enable MSC and Controller
5.00	Start Ramp of the Speed Reference

4.2 Simulation Results

The simulations results are classified into two groups such as 1. Soft Start Operation of the DFIM and 2. Initial Rotor Position Correction.

4.2.1 Soft Start Operation of the DFIM

The simulation results begin with the stator current waveform while connecting to the grid as shown in Fig. 20. This connection resembles a transformer under no load condition, leading to an inrush current during the initial connection. This inrush can reduce lifespan of the motor, and it is considered the weak point of this starting method when it is applied to a large size DFIM. Therefore, various techniques; for example, pre-insertion resistor, sequential energization, and series reactors, to mitigate the inrush current is required. However, the inrush current does not appear in this simulation due to the use of the linear WRIM model which does not include magnetic saturation.

At the time 1.5 s, the process of the stator flux estimation is started. This process requires about 0.2 s. to reach a steady state. In this process, two conditions were performed, $i'^{e}_{rd} = 0$ and $i'^{e}_{rd} = \left|\vec{i}^{e}_{ms}\right|$, to investigate the differences in the stator flux waveform estimated.

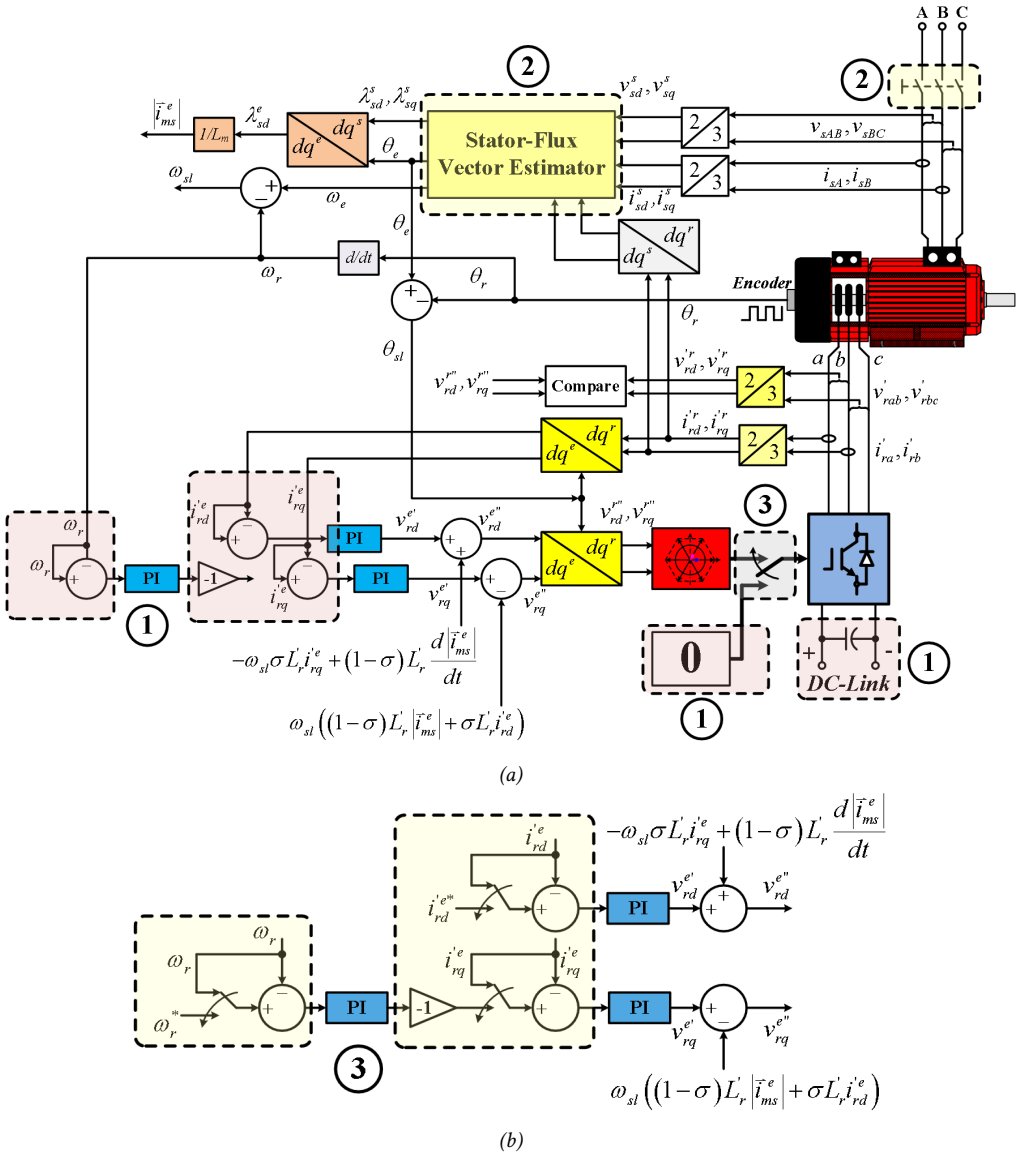

***Fig. 17**: Control Diagram Showing (a) the Operating Sequence for the Soft Start Operation from Step 1 to Step 3 and (b) Change in Controller Reference at Step 3.*

The results are shown in Figs. 21 and 22 respectively. The results before the time 2 s. are only affected by the stator current, but from 2 s., the effect of the rotor current is involved. The results shown in Figs. 23 and 24 are the stator and rotor current waveforms focusing on the time that the MSC is enable and the rotor d-axis current reference is set (Step 3). Two cases are presented here, $i'^{e}_{rd} = 0$ and $i'^{e}_{rd} = \left|\vec{i}^{e}_{ms}\right|$.

Considering the results shown in Figs. 23 and 24 together with the results shown in Figs. 21 and 22, the stator flux linkage waveforms remain the same in both conditions following equation (5).

The DFIM is fully energized and ready to start. The speed is first set to zero and then start accelerating at the time 5 s. It is accelerating from standstill to 1.2 pu. speed which is in the super synchronous speed region. In this simulation, the DFIM was controlled to energized via the stator circuit only. The speed profile during acceleration at different acceleration rates is shown in Fig. 25. The waveform of an electromagnetic torque with a ramp rate at 0.1 pu./s is also presented along with the speed profile in Fig. 26.

As shown in this figure, the torque is step up to overcome the load torque resulting in rotor acceleration. The final torque is slightly higher than the initial torque due to the viscous friction of the system. The simulation results under the same constant load at 0.5 pu. at different acceleration rates are shown in Figs. 27 – 29. It can be observed that the accelerating torque is inversely proportional to the acceleration time as shown in the speed and torque curves in Fig. 27.

The results shown in Figs. 28 and 29 are the stator current and rotor current waveforms in the stator

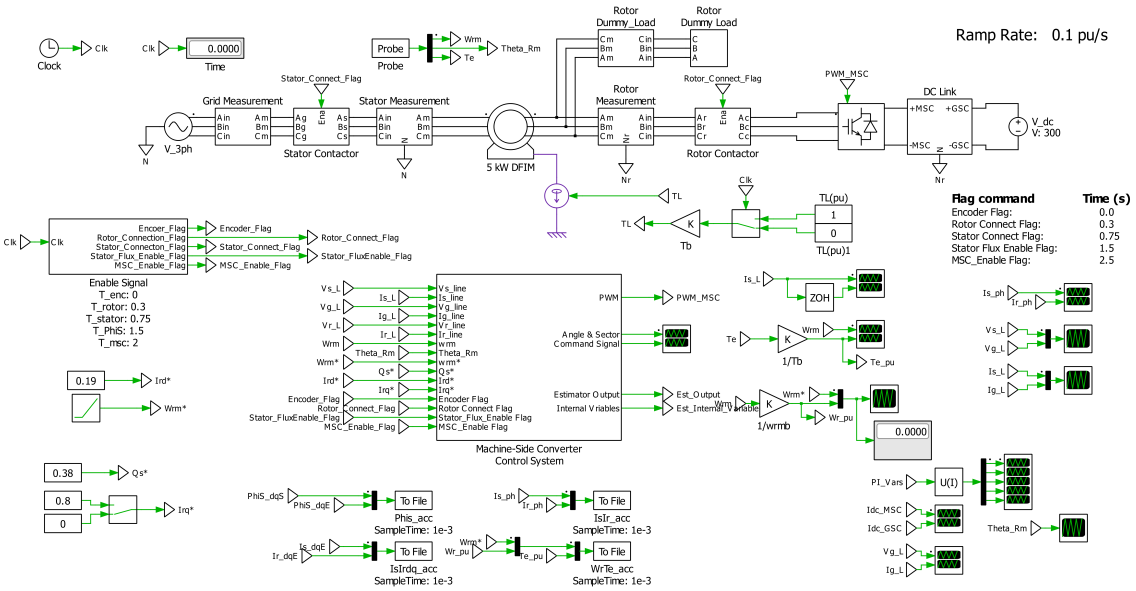

***Fig. 18**: Simulation Diagram for the Proposed Operation of the DFIM.*

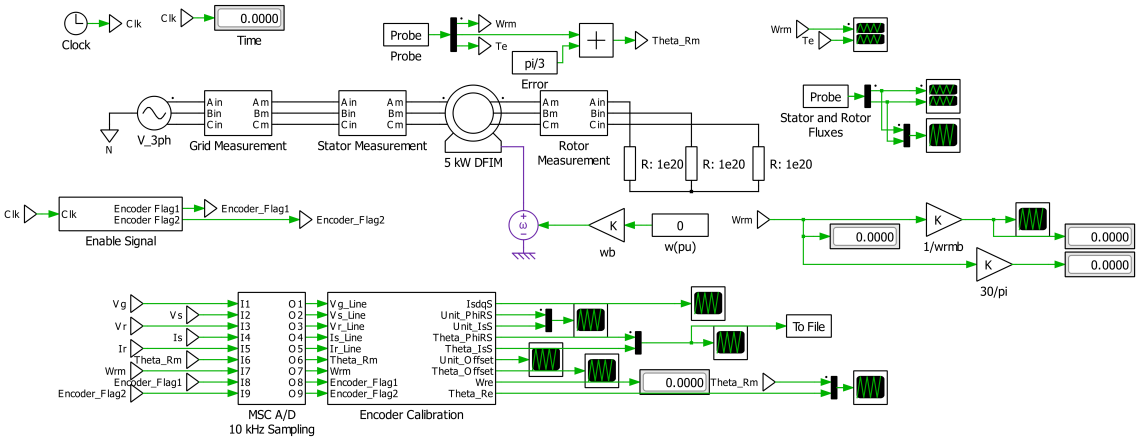

***Fig. 19**: Simulation Diagram for Initial Rotor Position Correction.*

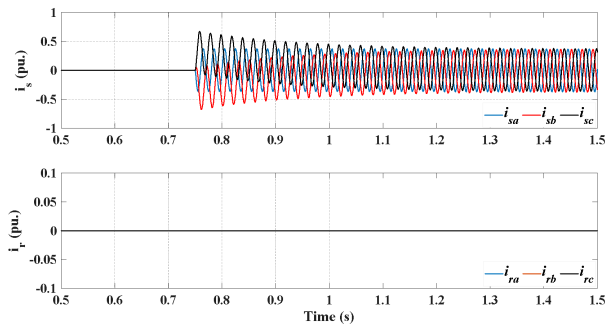

***Fig. 20**: Simulation Results Showing (Top) Stator Current and (Bottom) Rotor Current Waveforms while Connecting the Stator to the Grid.*

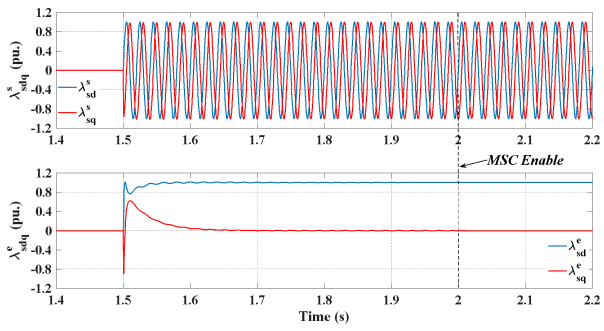

***Fig. 21**: Simulation Results Showing the Waveforms of Stator Flux in the Stationary Reference Frame Fixed to Stator (Top) and the Stator Flux Reference Frame (Bottom) while Enabling Stator Flux Estimation and $i'^{e}_{rd} = 0$.*

flux reference frame during acceleration at different acceleration rates. The torque is reflected on the q-axis rotor and stator currents as described in equations (8) and (17). Meanwhile, the stator flux is reflected on the d-axis rotor and stator currents following equation (7).

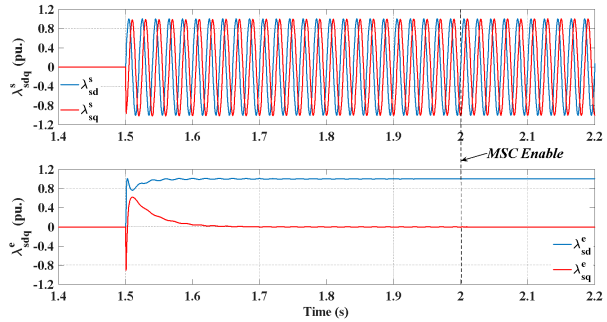

***Fig. 22**: Simulation Results Showing the Waveforms of Stator Flux in the Stationary Reference Frame fixed to Stator (Top) and the Stator Flux Reference Frame (Bottom) while Enabling Stator Flux Estimation and* $i'^{e}_{rd} = \left|\vec{i}^{\,e}_{ms}\right|$.

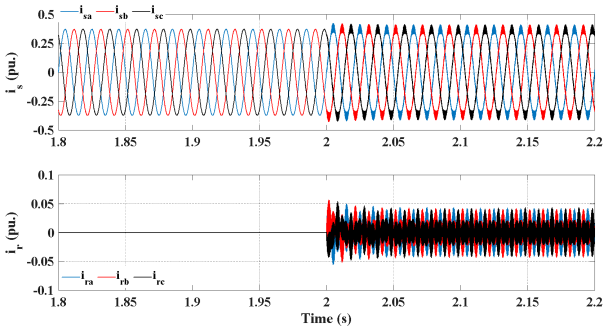

***Fig. 23**: Simulation Results Showing (Top) the Stator Current and (Bottom) Rotor Current Waveforms while Enabling the MSC with* $i'^{e}_{rd} = 0$.

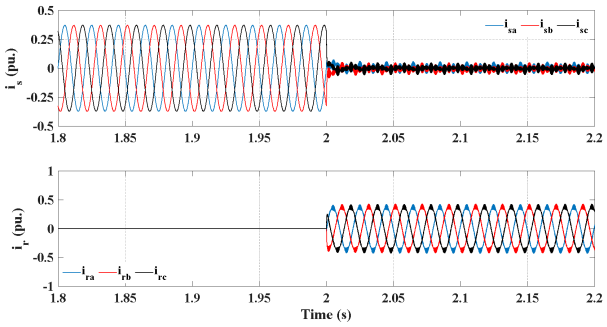

***Fig. 24**: Simulation Results Showing (Top) the Stator Current and (Bottom) Rotor Current Waveforms while Enabling the MSC with* $i'^{e}_{rd} = \left|\vec{i}^{\,e}_{ms}\right|$.

Moreover, the three-phase current waveforms of both stator and rotor are shown Fig. 30. It can also be observed that the phase sequence of the rotor currents changes when the rotor speed pass through the synchronous speed.

The last set of the simulation results is about the effect of load torque on the electromagnetic torque, the stator current, the rotor current and the stator flux linkage. The

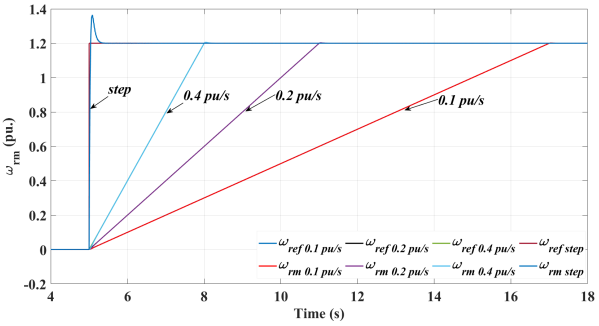

***Fig. 25**: Simulation Results Showing the Waveforms of the Reference Speed and the Actual Speed of the Rotor while Accelerating at Different Rates.*

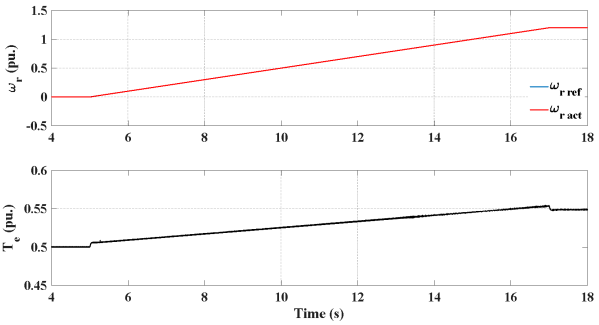

***Fig. 26**: Simulation Results Showing the Waveforms of (Top) the Reference Speed and the Actual Speed of the Rotor and (Bottom) Electromagnetic Torque while Accelerating with 0.5pu. Load at 0.1 pu./s. Ramp Rate.*

results are shown in Figs. 31 to 34. Considering the rotor current and stator current waveforms in Figs. 32 and 33 respectively, the d-axis rotor current is controlled to be zero, so the DFIM is fully excited via the stator circuit only. The d-axis stator current is equal to the stator magnetizing current following equations (7) and (29). However, the d-axis stator currents under different loads are not the same due to the voltage drop across the stator resistance. For the q-axis component, the sign of the rotor currents and the stator currents are different following equation (8).

Likewise, the d-axis component of the stator flux linkage in Fig. 34, tends to be lower when the load torque becomes higher. This reduction in stator flux is due to an increase in the voltage drop across the stator resistance proportional to an increase in stator current.

4.2.2 Initial Rotor Position Correction

The simulation results of this part are presented in Figs. 35 to 38. In the simulation, the initial rotor position was set to zero while the measured rotor position was offset by ±60 degrees. These angles are the mechanical angles, so the differences between the calibrated angle $\theta_{\lambda v}(t)$ the reference angle $\theta_{\lambda i}(t)$ becomes ±120 degrees.

Two different speed conditions were simulated, at standstill and 0.1pu speed (150 rpm). Ideally, the WRIM

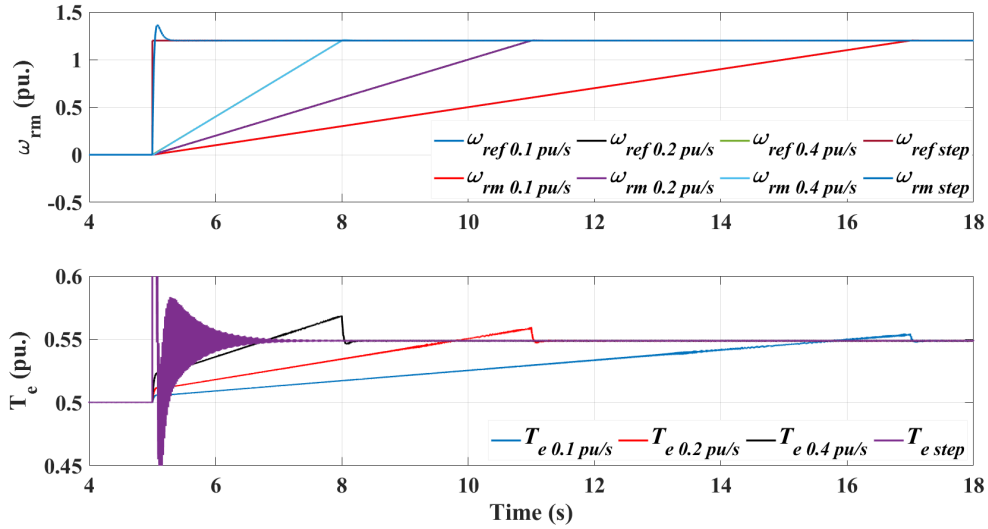

***Fig. 27**: Simulation Results Showing the Waveforms of (Top) the Reference Speed and the Actual Speed of the Rotor and (Bottom) the Electromagnetic Torque while Accelerating with 0.5pu. Load at Different Ramp Rates.*

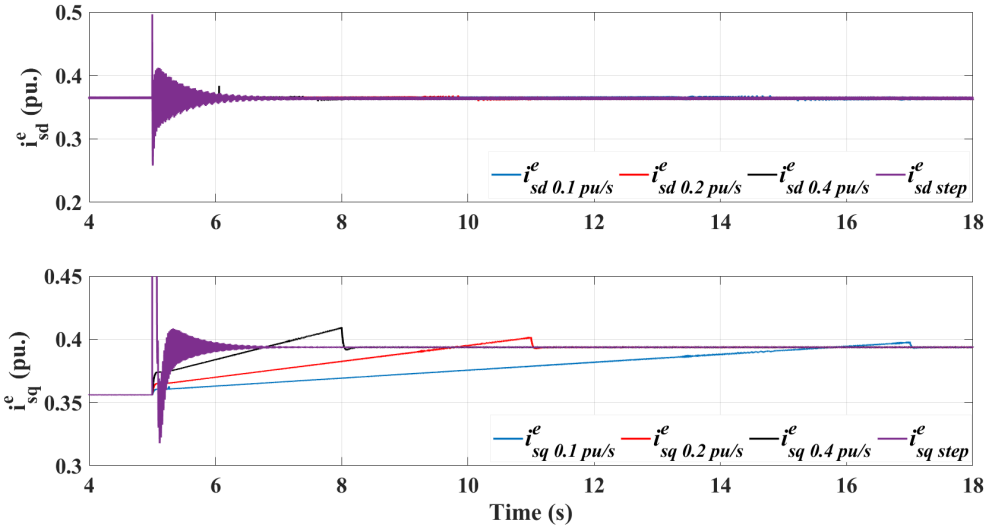

***Fig. 28**: Simulation Results Showing the Waveforms of (Top) the D-Axis Stator Current and (Bottom) the Q-Axis Stator Current in the Stator Flux Reference Frame while Accelerating with 0.5pu. Load at Different Ramp Rates.*

supplied by a three-phase source at the stator while leaving the rotor open-circuited results in zero speed condition. However, in practice, especially under no-load condition, the rotor can rotate at slow speed caused by the reluctance torque due to the slot-opening of the rotor. Therefore, the simulations at two different speed conditions were performed to cover the possible cases.

Figs. 35 and 36 are the simulation results at 0.1 pu. speed. The top waveforms of both figures are the rotor electrical angle. It changes periodically indicating that the rotor is rotating. The bottom waveforms are the waveforms of the reference rotor position in stationary $\theta_{\lambda i}(t)$and the waveform of rotor that need to be corrected$\theta_{\lambda v}(t)$. Before the time 2 s., the $\theta_{\lambda v}(t)$was not yet corrected, the values of $\Delta\theta_r$ are $\pm$120 degrees as depicted in both figures. After the time 2 s., $\theta_{\lambda v}(t)$ was corrected, so, following equation (30), the $\theta_{\lambda v}(t)$ coincides with the $\theta_{\lambda i}(t)$. It can also be observed that the value of $\theta_r(t)$ change abruptly for 120 degrees ($\frac{2\pi}{3}$ rad.) at the time 2 s. resulting in $\theta_r(t)$ at 0 degree.

The results shown in Figs. 37 and 38 are the simulation results at standstill. The values of the $\theta_r(t)$ are constant throughout the simulation. The correction was performed at the time 2 s., so the $\theta_r(t)$ changes to 0 degrees at this time for both cases.

It should be noted that, the initial rotor position is required only one time when the system is first setup, or when the encoder is re-installed. Once the correction complete, the compensated value, θ_{r_comp}, can be programmed in the firmware for further operations.

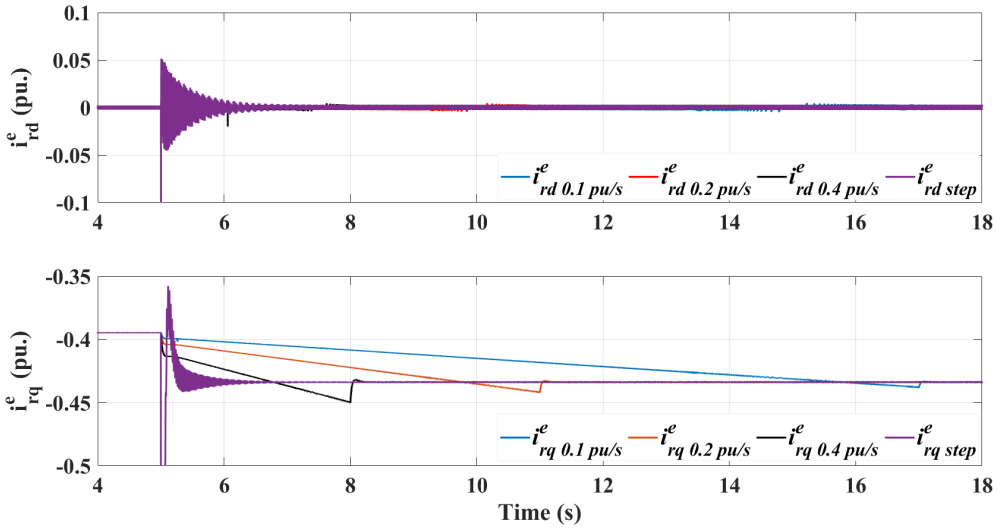

***Fig. 29**: Simulation Results Showing the Waveforms of (Top) the D-Axis Rotor Current and (Bottom) the Q-Axis Rotor Current in the Stator Flux Reference Frame while Accelerating with 0.5pu. Load at Different Ramp Rates.*

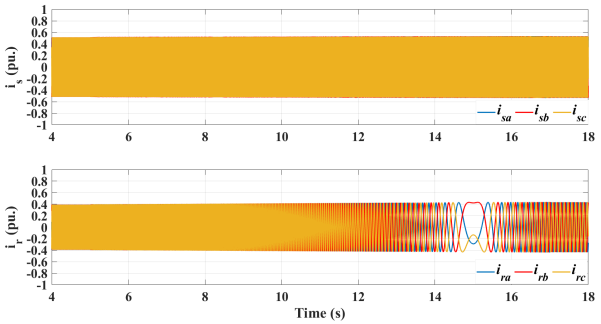

***Fig. 30**: Simulation Results Showing the Waveforms of (Top) the Three-Phase Stator Current and (Bottom) the Rotor Current while Accelerating with 0.5 pu. Load at 0.1 pu/s. Ramp Rate.*

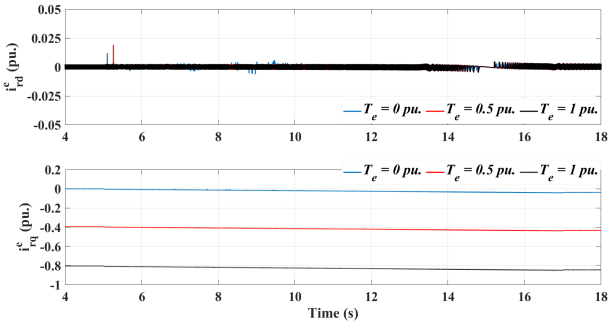

***Fig. 32**: Simulation Results Showing the Waveforms of (Top) the D-Axis Rotor Current and (Bottom) the Q-Axis Rotor Current in the Stator Flux Reference Frame while Accelerating with Different Loads. at 0.1 pu./s. Ramp Rate.*

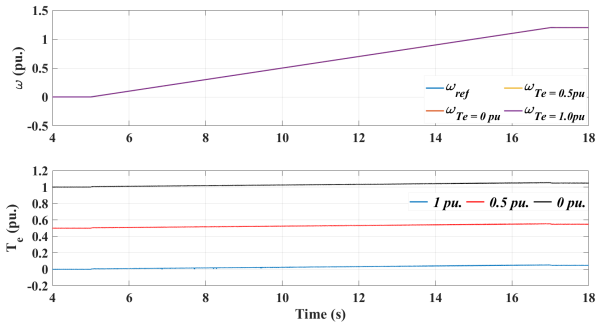

***Fig. 31**: Simulation Results Showing the Waveforms of (Top) the Reference Speed and Actual Speed of the Rotor and (Bottom) the Electromagnetic Torque while Accelerating with Different Loads at 0.1 pu/s. Ramp Rate.*

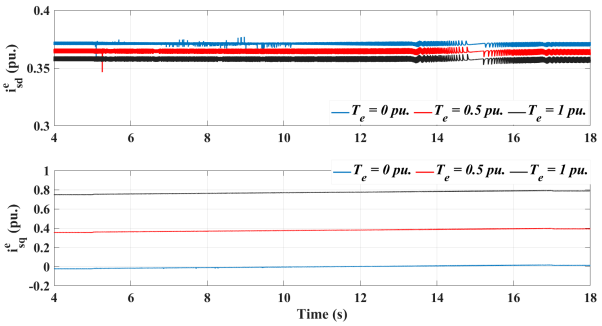

***Fig. 33**: Simulation Results Showing the Waveforms of (Top) the D-Axis Stator Current and (Bottom) the Q-Axis Stator Current in the Stator Flux Reference Frame while Accelerating with Different Loads at 0.1 pu/s. Ramp Rate.*

5. CONCLUSIONS

The soft start from a standstill of a DFIM based on stator flux vector control and the conventional topology is proposed in this paper. A proper operating sequence is required to achieve the control of the MSC to control the DFIM at standstill. Once the MSC is enabled, the motor

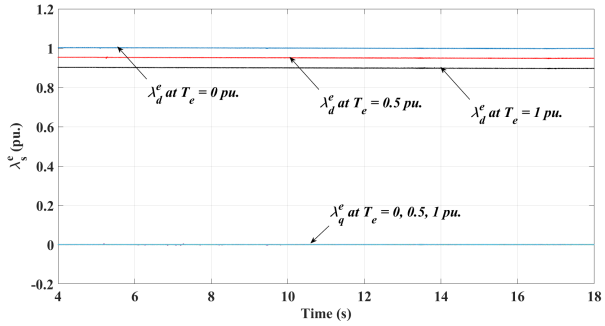

***Fig. 34**: Simulation Results Showing the Waveforms of (Top) the D-Axis Stator Flux and (Bottom) the Q-Axis Stator Flux in the Stator Flux Reference Frame while Acceleration with Different Loads at 0.1 pu/s. Ramp Rate.*

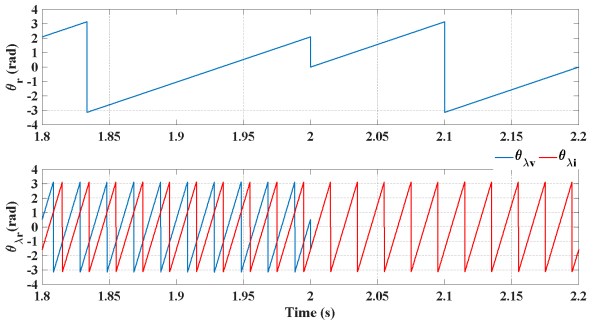

***Fig. 35**: Simulation Results Showing the Waveforms of (Top) the Rotor Electrical Angle and (Bottom) $\theta_{\lambda v}(t)$ and $\theta_{\lambda i}(t)$ when the $\theta_{\lambda v}(t)$ Leads the $\theta_{\lambda i}(t)$ for 120 Degrees under Calibration at 0.1 pu. Speed.*

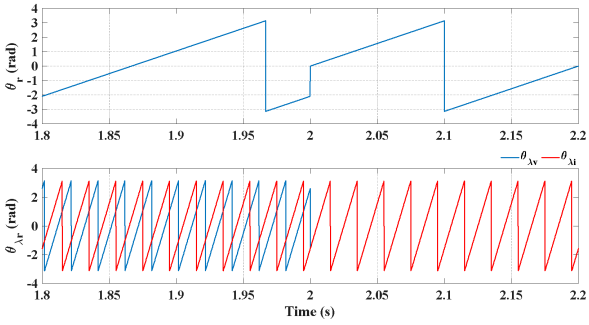

***Fig. 36**: Simulation Results Showing the Waveforms of (Top) the Rotor Electrical Angle and (Bottom) $\theta_{\lambda v}(t)$ and $\theta_{\lambda i}(t)$ when the $\theta_{\lambda v}(t)$ Lags the $\theta_{\lambda i}(t)$ for 120 Degrees under Calibration at 0.1 pu. speed.*

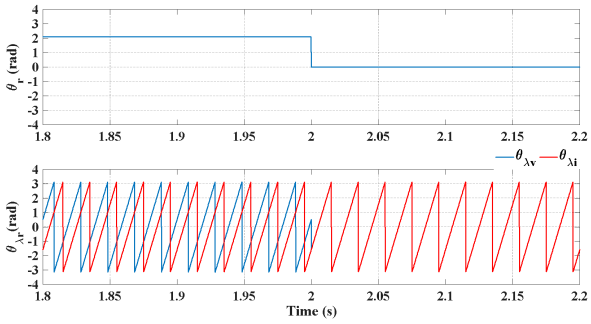

***Fig. 37**: Simulation Results Showing the Waveforms of (Top) the Rotor Electrical Angle and (Bottom) $\theta_{\lambda v}(t)$ and $\theta_{\lambda i}(t)$ when the $\theta_{\lambda v}(t)$ Leads the $\theta_{\lambda i}(t)$ for 120 Degrees under Calibration at Standstill.*

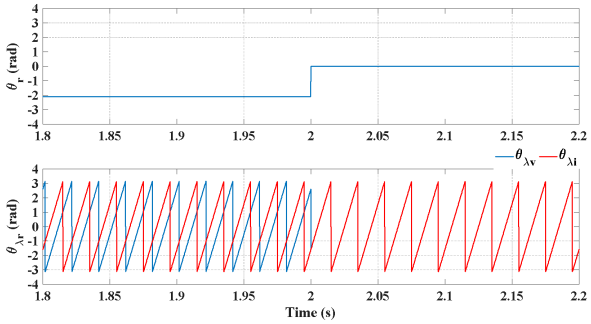

***Fig. 38**: imulation Results Showing the Waveforms of (Top) the Rotor Electrical Angle and (Bottom) $\theta_{\lambda v}(t)$ and $\theta_{\lambda i}(t)$ when the $\theta_{\lambda v}(t)$ Lags the $\theta_{\lambda i}(t)$ for 120 Degrees under Calibration at Standstill.*

speed can be fully controlled. Regarding the converter size as in the case of the DFIG, the application is limited to variable torque loads such as pumps and blowers. However, the DFIM can operate at any the speed up to twice the base speed with constant flux operation regardless of the converter size. In addition, this paper presents an alternative method for correcting the initial rotor position based on rotor flux vector. This method can be performed at any speed, and it is particularly suitable at zero speed as the DFIM normally starts from standstill.

All simulations were performed using PLECS software and the simulation results are plotted using MATLAB software. The simulation results are classified based on the operating step shown in Section 3. The simulation started from connecting the stator to the three-phase source while leaving the rotor open circuit. The process of enabling the stator flux linkage was then performed. The stator flux linkage waveforms under different values of the d-axis rotor current are illustrated. The stator flux waveforms under two conditions are the same because the stator flux vector is the combination of both stator and rotor currents. Change in one current affects another current as discussed in equation (15) but does not affect the flux linkage.

The MSC was then connected to the rotor circuit, and it started operation following the operation criteria discussed in Section 3. During the acceleration, the simulations were performed at different acceleration rates ranging from 0.1 pu/s to step command. The results show that the DFIM can operate successfully through super-synchronous speed region based on stator flux vector control. No change in either control method or topology is required. It can be observed that the

electromagnetic torque after acceleration is higher than that before acceleration. This difference is due to the viscous friction which is proportional to the speed of the rotor. Simulations under different loads were also performed. The simulation results follow the theory as described in Section 2. It should be noted that the stator flux decreases due to an increase in the voltage drop across stator resistance which is proportional to an increase in stator current. A drawback of this method is the inrush current while connecting the stator to the three-phase source while the rotor is open circuited. However, it can be mitigated by the method applied to start the three-phase transformers.

In the case of the proposed initial rotor position correction, the simulation started from connecting the stator to the three-phase source while leaving the rotor open circuited. This method is designed to correct the rotor position at standstill based on the rotor flux vector equation. However, the simulations were performed under two different conditions, low-speed and zero speed, to cover the possible conditions that can occur. The simulation results show that this method can successfully correct the rotor position under both conditions regardless of the sign of error position. It can also be applied at any speed, for example, in the case that the rotor is driven by the prime mover. Practically, this method is designed to correct the rotor position when setting up the system or re-installing the encoder. The compensating angle can be included in the firmware of the controller for further operation.

All simulations were performed based on C-Script as practically coded in the real system. Therefore, the algorithm and code can be adapted to the microcontroller for implementation with little modification. Finally, it can be concluded that the proposed startup method has successfully validated the hypothesis of starting the DFIM without either circuit reconfiguration or change in MSC control method. Likewise, the decoupled control resulting from the stator flux vector control is maintained in every speed region.

REFERENCES

[1] W. Leonhard. *Control of Electrical Drives*, 3rd ed. Berlin, Germany: Springer, 2001.

[2] R. Pena, J. C. Clare, and G. M. Asher, "Doubly-Fed Induction Generator Using Back-to-Back PWM Converters and Its Application to Variable Speed Wind-Energy Generation", *IEE Proceeding of Electric Power Applications*, vol. 143, no. 5, pp. 380-387, 1996.

[3] G. Tapia, G. Santamaria, M. Telleria, and A. Susperregui, "Methodology for Smooth Connection of Doubly Fed Induction Generators to the Grid," *IEEE Transactions on Energy Conversion*, vol. 24, no. 4, pp. 959-971, Dec 2009.

[4] S. Muller, M. Deicke, and R. W. De Doncker, "Doubly Fed Induction Generator Systems for Wind Turbines," *IEEE Industry Applications Magazine*, vol. 8, no. 3, pp. 26–33, May.-Jun. 2002.

[5] B. Wu, Y. Lang, N. Zargari, and S. Kouro. *Power Conversion and Control of Wind Energy Systems*. Hoboken, NJ, USA: Wiley, 2011.

[6] M. Debbou, A. Damdoum, and M. P.-David, "Optimal Sliding Mode Control for DFIM Electric Marine Thruster," in *Proceedings of the International Conference on Electrical System for Aircraft, Railway, Ship Propulsion and Road Vehicles & International Transportation Electrification Conference (ESARS-ITEC)*, Nov. 2016, pp. 1–6.

[7] M. Debbou and M. Pietrzak-David, "Novel Tolerant Fault DFIM Drive for Naval Propulsion," in *Proceedings of the. 39th Annual Conference of the IEEE Industrial Electronics Society (IECON 2013)*, Nov. 2013, pp. 3006–3011.

[8] Y. Pannatier, B. Kawkabani, C. Nicolet, A. Schwery and J. . -J. Simond, "Start-Up and Synchronization of a Variable Speed Pump-Turbine Unit in Pumping Mode," in *The XIX International Conference on Electrical Machines - ICEM 2010*, Rome, Italy, 2010, pp. 1-6.

[9] Y. Pannatier, B. Kawkabani, C. Nicolet, J. -J. Simond, A. Schwery and P. Allenbach, "Investigation of Control Strategies for Variable-Speed Pump-Turbine Units by Using a Simplified Model of the Converters," *IEEE Transactions on Industrial Electronics*, vol. 57, no. 9, pp. 3039-3049, Sept. 2010.

[10] X. Yuan, J. Chai, and Y. Li, "A Converter-Based Starting Method and Speed Control of Doubly-Fed Induction Machine With Centrifugal Loads," *IEEE Transaction on Industry Applications*, vol. 47, no. 3, pp. 1409–1418, May/Jun. 2011.

[11] Y. Pannatier, B. Kawkabani, C. Nicolet, A. Schwery and J. . -J. Simond, "Optimization of the Start-Up Time of a Variable Speed Pump-Turbine Unit in Pumping Mode," in *2012 XXth International Conference on Electrical Machines*, Marseille, France, 2012, pp. 2126-2132.

[12] T. Maendly, A. Hodder and B. Kawkabani, "Start-Up of a Varspeed Group in Pump Mode, Practical Implementations and Tests," in *2016 XXII International Conference on Electrical Machines (ICEM)*, Lausanne, Switzerland, 2016, pp. 1201-1207.

[13] A. Joseph, R. Selvaraj, T. R. Chelliah, and S.V. Appa Sarma, "Starting and Braking of Large Variable Speed Hydrogenerating Unit Subjected to Converter and Sensor Faults," *IEEE Transactions on Industry Applications*, vol. 54, no. 4, pp. 3372–3382, Jul.-Aug. 2018.

[14] T. Zhao, D. Xiang and, and Y. Sheng, "An Approach to Start a Shaft Generator System Employing DFIM under Power Take Me Home Mode," in *2018 IEEE International Power Electronics and Application Conference and Exposition (PEAC)*, Shenzhen, China, 2018, pp. 1-5.

[15] J. Zhao, H. Li, X. Xiang and W. Li, "Research

on Startup and Emergency Braking Strategy of Doubly-Fed Induction-Machine-Based Flywheel Energy Storage System," in *2023 26th International Conference on Electrical Machines and Systems (ICEMS)*, Zhuhai, China, 2023, pp. 4971-4976.

[16] M. Narayanasamy and Y. Sukhi, "Rotor Short Circuited Start-up Strategy for a Doubly-Fed Induction Machine-fed Large-Variable-Speed Pumped Storage Unit Operating in Pumping Mode," *Journal of Power Electronics*, vol. 23, pp. 1733–1744, 2023.

[17] A. Banerjee, M. S. Tomovich, S. B. Leeb, and J. L. Kirtley, "Control Architecture for a Switched Doubly Fed Machine Propulsion Drive," *IEEE Transactions on Industry Applications*, vol. 51, no. 2, pp. 1538–1550, Mar-Apr. 2015.

[18] A. Banerjee, M. S. Tomovich, S. B. Leeb and J. L. Kirtley, "Power Converter Sizing for a Switched Doubly Fed Machine Propulsion Drive," *IEEE Transactions on Industry Applications*, vol. 51, no. 1, pp. 248-258, Jan.-Feb. 2015.

[19] Y. Zhang and B. T. Ooi, "Adapting DFIGs for Doubly-Fed Induction Motors Operation," in *2012 IEEE Power and Energy Society General Meeting*, San Diego, CA, USA, 2012, pp. 1-8.

[20] M. Bodson and M. A. Hossain, "Integrated Control of a Motor/Generator Set Composed of Doubly Fed Induction Machines," *IEEE Journal of Emerging and Selected Topics in Power Electronics*, vol. 8, no. 2, pp. 1858-1869, June 2020.

[21] G. peng, K.Ni, C.Gan, R. Qu, and Y. Hu, "A Direct Starting Method of Doubly-Fed Induction Machine for Shipboard Propulsion System Application," in *2021 24th International Conference on Electrical Machines and Systems (ICEMS)*, Gyeongju, Korea, Republic of, 2021, pp. 949-954.

[22] T. Kawabata, Y. Kawabata, and K. Nishiyama, "New Configuration of High-Power Inverter Drives," in *Proceedings of IEEE International Symposium on Industrial Electronics*, Warsaw, Poland, vol. 2, 1996, pp. 850–855.

[23] Y. Kawabata, E. C. Ejiogu, K. Nishiyama and T. Kawabata, "High-Power Drive Using a Wound Rotor Induction Motor and Two Current Controlled Inverters," in *Proceedings of Power Conversion Conference - PCC '97*, Nagaoka, Japan, vol. 2, 1997, pp. 579-582.

[24] Y. Kawabata, E. Ejiogu, and T. Kawabata, "Vector-Controlled Double Inverter-Fed Wound-Rotor Induction Motor Suitable for High-Power Drives," *IEEE Transactions on Industry Applications*, vol. 35, no. 5, pp. 1058–1066, Sep.-Oct. 1999.

[25] G. Poddar and V. T. Ranganathan, "Sensorless Field-Oriented Control for Double-Inverter-Fed Wound-Rotor induction motor drive," *IEEE Transactions on Industrial Electronics*, vol. 51, no. 5, pp. 1089–1096, Oct. 2004.

[26] G. Poddar and V. T. Ranganathan, "Direct Torque and Frequency Control of Double-Inverter-Fed Slip-Ring Induction Motor Drive," *IEEE Transactions on Industrial Electronics*, vol. 51, no. 6, pp. 1329-1337, Dec. 2004.

[27] F. Bonnet, P. -E. Vidal, and M. Pietrzak-David, "Dual Direct Torque Control of Doubly Fed Induction Machine," *IEEE Transactions on Industrial Electronics*, vol. 54, no. 5, pp. 2482-2490, Oct. 2007.

[28] Y. Liu and L. Xu, "The Dual-Current-Loop Controlled Doubly Fed Induction Motor for EV/HEV Applications," *IEEE Transaction on Energy Conversion*, vol. 28, no. 4, pp. 1045–1052, Dec. 2013.

[29] M. Abdellatif, M. Debbou, I. S.-Belkhodja, and M. P. David, "Simple Low-Speed Sensorless Dual DTC for Double Fed Induction Machine Drive," *IEEE Transactions on Industrial Electronics*, vol. 61, no. 8, pp. 3915–3922, Aug. 2014.

[30] V. V. Reddy, N. Aarzoo, G. Poddar and S. Sau, "Improved Sensorless Operation of Double Inverter Fed Wound Rotor Induction Machine with Seamless Mode Transitions," *IEEE Transactions on Industrial Electronics*, vol. 70, no. 11, pp. 11078-11086, Nov. 2023.

[31] L. S. Barik and H. Misra, "Dual Side Field Oriented Control of Slip Ring Induction Motor," *IEEE Transactions on Industrial Electronics*, Early Access, May. 2024.

[32] A. Nanda and V. S. S. P. K. Hari, "Dual Volts-per-Hertz Control of Double-Inverter-Fed Wound Rotor Induction Machine," *IEEE Transactions on Industrial Electronics*, vol. 71, no. 3, pp. 2198–2207, Mar. 2024.

[33] A. Nanda and V. S. S. P. K. Hari, "Improved Dual Volts-Per-Hertz Control of Double Inverter-Fed Wound Rotor Induction Machine," *IEEE Transactions on Industrial Electronics*, vol. 71, no. 9, pp. 10268-10276, Sept. 2024.

[34] Patrick L. Jansen and Robert D. Lorenz, "A Physical Insightful Approach to the Design and Accuracy Assessment of Flux Observers for Field Oriented Induction Machine Drives," *IEEE Transactions on Industry Applications*, vol. 30, No. 1, pp. 101-110, Jan.-Feb 1994.

[35] Cristian Lascu, Ion Boldea, and Frede Blaabjerg, "A Modified Direct Torque Control for Induction Motor Sensorless Drive," *IEEE Transactions on Industry Applications*, vol. 36, no. 1, pp. 122-130, Jan.-Feb 2000.

[36] Z. Ali, N. Christofides, L. Hadjidemetriou, E. Kyriakides, Y. Yang and F. Blaabjerg, "Three-phase Phase-Locked Loop Synchronization Algorithms for Grid-Connected Renewable Energy Systems: A Review," *Renewable and Sustainable Energy Reviews*, vol. 90, pp. 434-452, July 2018.

Warachart Suwan-ngam received the B.Eng. and M.Eng. in Electrical Engineering from the King Mongkut's Institute of Technology Ladkrabang (KMITL), Bangkok, Thailand in 1999 and 2002, respectively, and the Ph.D. in Electronic and Electrical Engineering from the University of Strathclyde, Glasgow, UK. in 2008. He is currently an Assistant Professor in the Department of Electrical Engineering, School of Engineering, KMITL. His research interests include electrical machines and AC drives, power electronics applications for renewable energy, condition monitoring and fault diagnosis for electrical machines and power converters, and DSP applications for AC drives and power electronics converters.